

Accurate Segmentation of Cervical Cytoplasm and Nuclei Based on Multiscale Convolutional Network and Graph Partitioning

Yuyi Song, Ling Zhang, Siping Chen, Dong Ni, Baiying Lei*, and Tianfu Wang*

Abstract—In this paper, a multiscale convolutional network (MSCN) and graph-partitioning-based method is proposed for accurate segmentation of cervical cytoplasm and nuclei. Specifically, deep learning via the MSCN is explored to extract scale invariant features, and then, segment regions centered at each pixel. The coarse segmentation is refined by an automated graph partitioning method based on the pretrained feature. The texture, shape, and contextual information of the target objects are learned to localize the appearance of distinctive boundary, which is also explored to generate markers to split the touching nuclei. For further refinement of the segmentation, a coarse-to-fine nucleus segmentation framework is developed. The computational complexity of the segmentation is reduced by using superpixel instead of raw pixels. Extensive experimental results demonstrate that the proposed cervical nucleus cell segmentation delivers promising results and outperforms existing methods.

Index Terms—Cervical segmentation, coarse to fine, graph partitioning, multiscale convolutional network (MSCN), touching-cell splitting.

I. INTRODUCTION

CERVICAL cancer is one of the common cancers leading to woman's morbidity and mortality [1]. More than 0.2 million people lose their life due to cervical cancer every year [2]. In 2008, 85% among 0.53 million new incidents of the cervical cancer has been found in the developing countries [3]. Pap smear is one of the easiest and most important examination [4] to significantly reduce the death rate of cervical cancer. The recently developed H&E stain is more stable and accurate compared with pap smear. Hence, cytology screening via H&E stain has been widely applied to detect early stages of cervical cancer

in the recent decade. However, such diagnosis is heavily dependent on the clinician's experience, which is extremely time consuming and is subjected to human error even for experienced doctors [5].

To address these issues, low-cost and efficient methods using computer technology have developed to assist doctor's analysis. This is particularly useful for underprivileged countries, which may not have access to highly experienced doctors. Therefore, development of new automated diagnosis techniques has been attracting numerous interest lately, which not only alleviates psychological fatigue of manual inspection, but also reduces the misdiagnosis and missed diagnosis [6]–[8].

Automatic-assisting methods have played an important role in nucleus detection of abnormal cervical cells [9], and great success has been witnessed for cervical cell segmentation [9]–[14]. Traditional methods assume the input image contains only a single cell so one boundary or at most two boundaries are considered. This assumption is not realistic as one cannot make any assumption about the number of cells. Besides, multiple touching cervical cell splitting is quite challenging. Complicated cases such as the irregular cross-lined leukocytes, dust, impurities, and uneven illumination make nucleus segmentation even more difficult. The existing touching nuclei splitting algorithms are not feasible, and cervical cell segmentation used in clinical application is still immature. In view of these challenges and limitations of the existing methods, it is essential to develop a new automatic tool for cervical nucleus and cytoplasm segmentation.

To obtain this goal, a multiscale convolutional network (MSCN) is investigated to densely extract a myriad of multiscale feature vectors for nucleus region detection [15]. To reduce segmentation complexity, superpixels are utilized instead of the raw pixels. In superpixels, similar pixels are clustered into regularly spacing. Hence, the texture, shape, and contextual information are also captured to evaluate the likelihood of a superpixel belonging to a certain part of the target structure. In addition, graph partitioning is also integrated with superpixels to refine the coarse segmentation [16]. Differing from the previous graph-partitioning method using only local statistical information, the global information is also integrated for improved segmentation.

To improve segmentation performance, touching cervical nuclei splitting plays a more significant role as compared to single cell segmentation. To achieve this goal, a marker via distance transform and adaptive threshold is constructed using an unsupervised clustering method instead of using concave points

Manuscript received January 28, 2015; revised April 8, 2015; accepted May 3, 2015. Date of publication May 7, 2015; date of current version September 16, 2015. This work was supported in parts by the National Natural Science Foundation of China under Grants 61402296, 61101026, 61372006, 81270707, and 61427806, the 48th Scientific Research Foundation for the Returned Overseas Chinese Scholars, National Natural Science Foundation of Guangdong Province under Grant S2013040014448, Shenzhen Key Basic Research Project JCYJ20130329105033277 and JCYJ20140509172609164, and Shenzhen-Hong Kong Innovation Circle Funding Program JSE201109150013A. Asterisk indicates corresponding author.

Y. Song, L. Zhang, S. Chen, and D. Ni are with Shenzhen University.

*B. Lei and *T. Wang are with the National-Regional Key Technology Engineering Laboratory for Medical Ultrasound, Guangdong Key Laboratory for Biomedical Measurements and Ultrasound Imaging, Department of Biomedical Engineering, School of Medicine, Shenzhen University, Shenzhen 518060, China (e-mail: leiby@szu.edu.cn; tfwang@szu.edu.cn).

Color versions of one or more of the figures in this paper are available online at <http://ieeexplore.ieee.org>.

Digital Object Identifier 10.1109/TBME.2015.2430895

applied by existing methods. This method is fast and has the capability to segment cells with or without unclear concave point. In addition, shape, color, and geometrical information are effectively incorporated to measure the evidence from different markers. According to some concave point, the touching nucleus is split based on the marker via shape and color information clustering. As a result, the limitations of the previous works such as poor stain, low contrast, and low illuminations are also resolved.

In this study, a deep-learning based method via the MSCN is developed for segmentation using a powerful feature representation. The main contributions of the proposed method are mainly fourfolds: 1) MSCN for the feature extraction; 2) graph partitioning for nucleus segmentation; 3) postprocessing via the prior knowledge; and 4) the touching nucleus splitting based on the marker.

II. RELATED WORK

A. Cervical Cell Segmentation

There is a myriad of the literature available for the cervical cytoplasm and nucleus splitting, which includes the widely used morphology operation [15], edge detection [14], k -means [11], [16], thresholding [12], [17], difference maximization [11], Hough transform [17], watershed [12], [18], [19], parameter fitting [20], and active contour model (ACM) [16], [21]. However, most of these approaches were developed for isolated cell only, hence such approaches are inapplicable for multiple nuclei splitting in the field-of-view images.

For segmenting cytoplasm and nuclei with multiple cells, Genctav *et al.* [12] proposed an unsupervised method for cervical cell segmentation using multiscale watershed. Bergmeir *et al.* [17] utilized the Canny edge operator to detect edges between the nucleus and cytoplasm first. Then, shape and prior knowledge were explored for cytoplasm boundary separation. Finally, the Hough transform was developed to localize the boundary for nucleus segmentation. Zhang *et al.* [13] proposed to segment the cytoplasm region with a multithresholding Otsu method. The nuclei were segmented using a local adaptive graph cut approach.

Although these methods can obtain good cytoplasm and nuclei segmentation performance, these methods were developed on healthy rather than a mix of pathological and healthy cells. Due to the difference in shape, size, chromatin among different pathological cells, these methods cannot be applied to nucleus segmentation when both healthy and cancerous cells are coexisting.

B. Convolutional Networks in Image Segmentation

The hierarchical representation based on the pixels, edgelets, motifs, parts, and objects has been extensively applied in the computer vision field. The convolutional neural network (CNN) is able to learn the hierarchical feature and provide a simple architecture [22], and hence, notable success has been achieved recently using the convolutional networks in the advanced computer vision, pattern recognition, image segmentation, object

retrieval, and object classification fields [23], [24]. For example, the CNN was applied for segmentation used in binary image restoration [25]. In [26], CNN segmented the H&E stained breast cancer using multichannel input. In [27], the deep CNN was implemented for neuronal membrane segmentation. In [22], feature extraction by the CNN was applied for scene labeling. In [28], an affinity graph for image segmentation was achieved by the deep learning method.

C. Segmentation by Graph Partitioning

The ACM and level set methods have been widely applied for image segmentation [29], [30], but these methods require individual initialization, shape prior, and contour knowledge, hence, the performance of these methods degrades when applied to intersecting objects without distinctive contours. Moreover, occlusion in objects degrades performance as well. As the pathological and healthy nuclei simultaneously exist with various shapes and sizes in full resolution H&E stained image, a large number of overlapping nuclei render proper initialization and shape definition to be quite challenging and impractical.

Graph partitioning is gaining popularity in the recent decade, and state-of-the-art performance [31], [32] is achieved with graph partitioning in the natural image field. Differing from the level set and ACM, the complexity of graph partitioning is not affected by the number of target objects. In the graph partitioning modeling, every node in the graph corresponds to the pixel, voxel, superpixel, or supervoxel [22], [33]. The nodes and edges of each graph [34], [35] are defined as the global objective function in graph partitioning approaches. By the max-flow/min-cut algorithm [36], the energy function is minimized to separate the foreground and background. The shape prior [37] learned from shape information [33] and manual annotation [38] can integrate the local image into the graph partitioning framework, and hence, more robust results are achieved.

D. Touching Nuclei Splitting

The splitting of touching nuclei is important for quantitative analysis of histopathological images because feature quantification is carried out on single cells before these cells are categorized using classification algorithms. The popular widely used touching nucleus splitting include the watershed [39], [40], gradient and edge detection [41], ACM [30], [42], morphological erosion [43], sliding band filter [44], and concave point [8], [45]–[47].

III. METHODOLOGY

A. MSCN Feature Representation and Coarse Segmentation

The traditional single scale convolutional network (SSCN) for segmentation suffers from two main problems: 1) different gray intensity information has a small distance in a small window, which cannot provide enough information for cell detection and 2) large window can achieve this goal but it is highly computational intensive. To tradeoff this, an MSCN method is investigated. The MSCN integrates large contexts into local decisions, but the parameter or dimensionality still remains

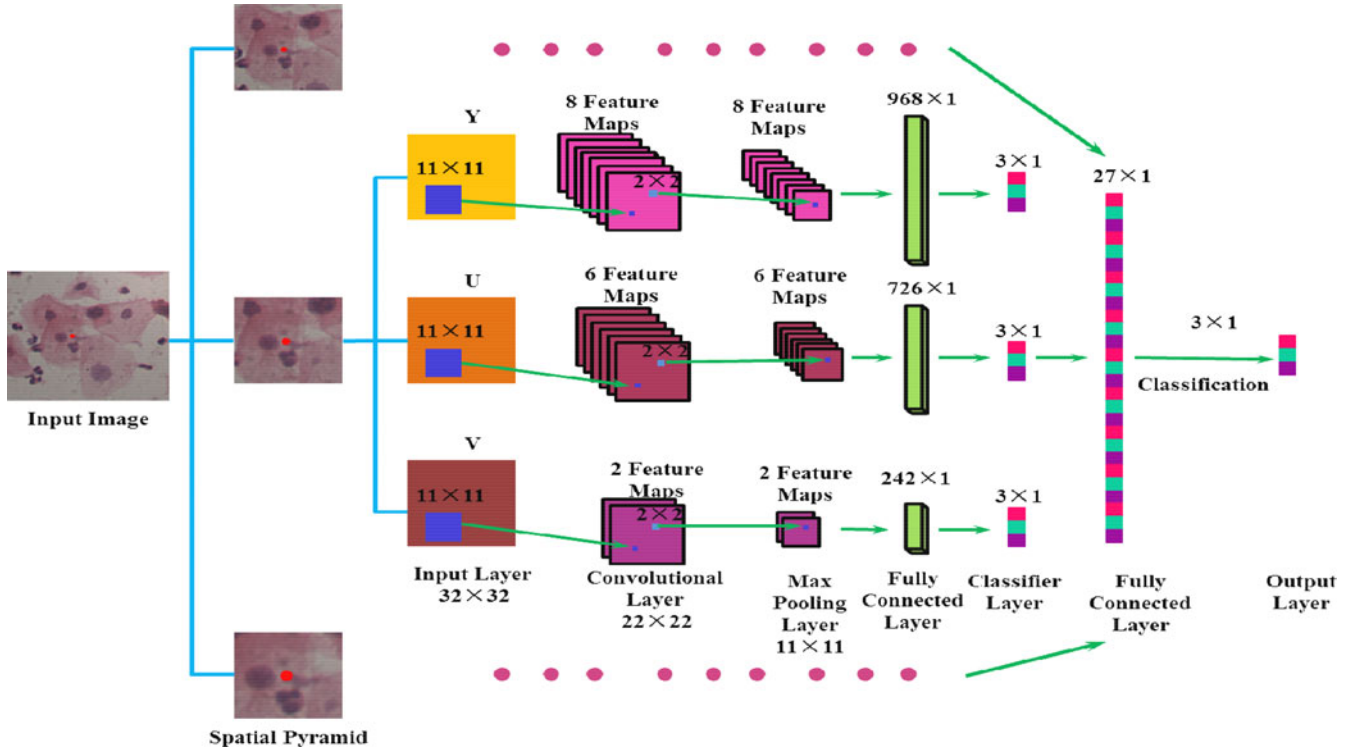


Fig. 1. Illustration of the MSCN structure.

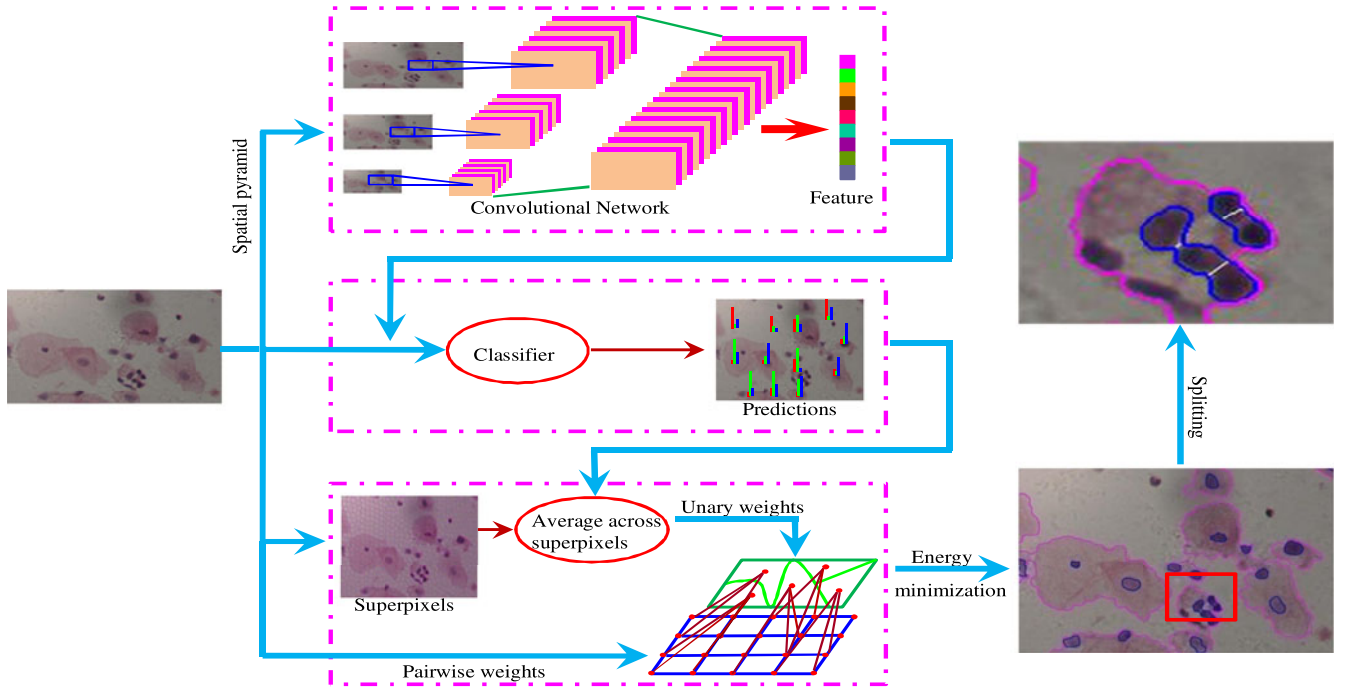


Fig. 2. Framework of the proposed segmentation system. Raw input image is transformed through a dyadic Gaussian pyramid. Each scale is fed to a one-stage convolutional network to generate a set of feature maps. The feature maps of all scales with a large contextual window around each pixel are concatenated together. The superpixel method is also explored based on the color and shape information. Final segmentation is produced by graph partitioning, and touching nucleus is separated by the marker.

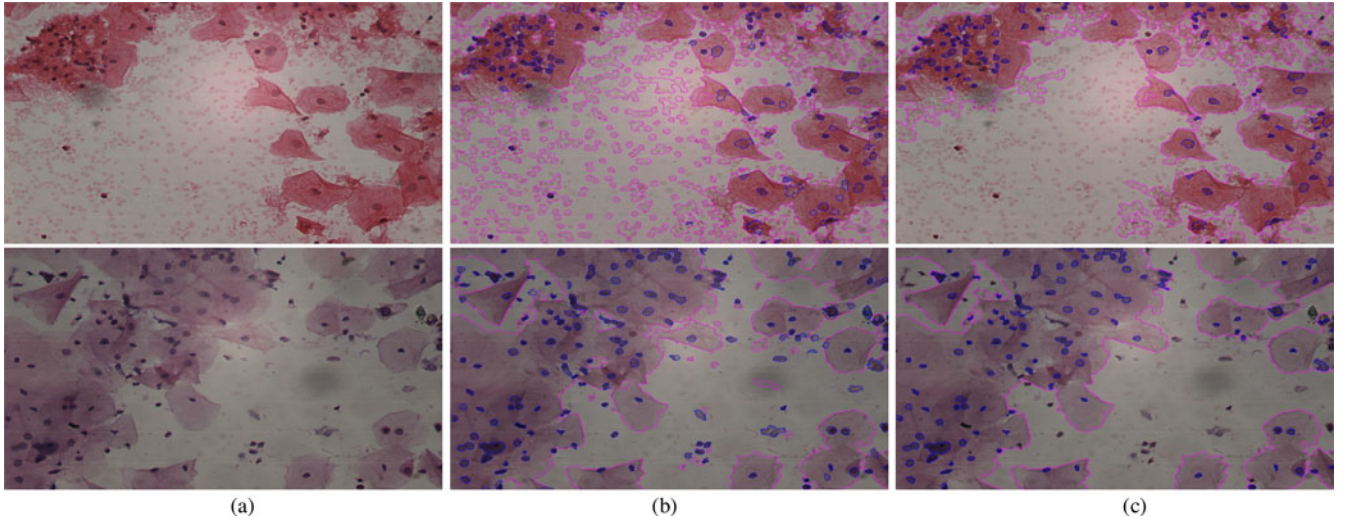


Fig. 3. (a) Color image with original resolution; (b) graph partitioning; (c) postprocessing. Boundaries of cytoplasm and nuclei delineated are marked as pink and blue, respectively.

manageable. The MSCN is composed of multistage trainable architecture and each stage includes a filter bank layer, nonlinearity layer, and feature pooling layer; the MSCN structure is illustrated in Fig. 1. Fig. 2 shows the detailed framework of our proposed method.

Specifically, for each input image I , a multiscale pyramid of images $I_s \forall s \in \{1, \dots, N\}$, is constructed using the dyadic Gaussian pyramids, where I_1 and I have the same size. For each scales, the image's raw pixels are used to train the MSCN. Given a classical convolutional network N_s with parameters ω_s , a network N_s with L layers, we have

$$N_s(I_s; \omega_s) = W_L H_{L-1} \quad (1)$$

where the vector of hidden units at layer l is

$$H_l = \text{pool}(\tanh(W_l H_{l-1} + b_l)). \quad (2)$$

For all $l \in \{1, \dots, L-1\}$, with b_l , a vector of bias parameters and $H_0 = I_s$, W_l are Toeplitz matrices. Each hidden unit vector H_l can be expressed as a regular convolution between kernels from W_l and the previous hidden unit vector H_{l-1} , squashed through a tanh function, and pooled spatially

$$H_{lp} = \text{pool}(\tanh(b_{lp} + \sum_{q \in \text{parents}(p)} W_{lpq} * H_{l-1,q})). \quad (3)$$

The filters W_l and biases b_l are trainable, in our experiments, the function tanh is a pointwise nonlinearity, pool is a function that we use max-pooling operator to take the maximum activation within the neighborhood.

The final feature extraction is based on N network output and upsampled to be the same size of f_1 .

$$F = [f_1, u(f_2), \dots, u(f_N)] \quad (4)$$

where u is the upsample function.

After feature extraction, a two-layer neural network is used to produce the correct categorization for all pixel locations i from

the feature vectors F_i .

$$y_i = W_2 \tanh(W_1 F_i + b_1) \quad (5)$$

where W_1 and W_2 are the trainable parameters of the classifier, b_1 is a vector of bias parameters. We compute the normalized predicted probability distributions over classes $\hat{C}_{i,a}$ by

$$\hat{C}_{i,a} = \frac{e^{y_{i,a}}}{\sum_{b \in \text{classes}} e^{y_{i,b}}}. \quad (6)$$

By minimizing the cross-entropy between predicted class distribution $\hat{C}_{i,a}$ and the target class distribution, Loss function penalizes their deviation and denoted as

$$\text{Loss} = - \sum_{i \in \text{pixels}} \sum_{a \in \text{classes}} C_{i,a} \ln(\hat{C}_{i,a}). \quad (7)$$

The true target probability $C_{i,a}$ of class a being present at location i is a hard target vector.

$$C_{i,a} = \begin{cases} 1, & i \in a, \\ 0, & \text{otherwise.} \end{cases} \quad (8)$$

Finally, a coarse segmentation is acquired to assign each pixel by maximizing the prediction at its location in pixel i .

$$P_i = \underset{a \in \text{classes}}{\text{argmax}} \hat{C}_{i,a}. \quad (9)$$

B. Fine Segmentation by Graph Partitioning

The resulting segmentation P , although fairly accurate, is not visually satisfying as it lacks spatial consistency, precise delineation of objects, and does not involve a global understanding of full image. In this section, we implemented a graph partitioning model to address this problem. Moreover, superpixels instead of pixels are implemented to reduce the computational cost and memory requirement.

1) *Superpixels*: To efficiently compute superpixel, the simple linear iterative clustering (SLIC) [48] method is selected due to the smoothed boundaries of the regular shape of images. SLIC takes advantage of the color similarity and the spatial information in the pixel to cluster the image. In SLIC, initial cluster centers are sampled on a regular grid. The center is first moved toward the lowest gradient position in a 3×3 neighborhood, iterative K -means clustering is then applied on the feature space that combines pixel locations and color information, the iteration continues until the distance between the new centers and previous ones is small enough.

2) *Graph Partitioning*: This method minimizes a global objective function defined on an undirected graph $G = (V, E)$, with vertices $v \in V$ and edge $e \in E \subseteq V \times V$. Each superpixel in the image is associated with a vertex, and each edge is added between every neighboring node. In our study, the energy function is defined as

$$E(y|x, \lambda) = \sum_{k \in V} \psi(y_k|x_k) + \lambda \sum_{(k,l) \in E} \phi(y_k, y_l|x_k, x_l) \quad (10)$$

where $y_k \in \{0, 1, 2\}$ is a class label assigned to superpixel k corresponding to the background, cytoplasm, and nucleus. The unary term ψ enforces the agreement between the node's label y_k and the prediction x_k , the pairwise term ϕ enforces regularity or local consistency between labels of neighboring node k and l , and the weight λ controls the relative importance of the two terms. The unary term is denoted as

$$\psi(y_k|x_k) = \exp(-\alpha \hat{D}_k) \quad (11)$$

where \hat{D}_k is the pixelwise distributions at superpixel k that are predicted from (9)

$$\hat{D}_{k,a} = \frac{1}{s(k)} \sum_{i \in k} P_{i,a} \quad (12)$$

where $s(k)$ denoting the area of superpixel k . The pairwise term is represented by

$$\phi(y_k, y_l|x_k, x_l) = \begin{cases} \exp(-\beta |\text{mean}_k - \text{mean}_l|), & y_k \neq y_l \\ 0, & \text{otherwise} \end{cases} \quad (13)$$

where mean_k is the mean intensity value within the superpixel k , details on the parameters λ, α, β shall be given in the experimental section of this paper. The energy is minimized using a fast min-cut/max-flow algorithm [36], [49].

3) *Postprocessing*: To reduce the errors due to the similarity about the blood, mucus, inflammatory cells, dust, powder, and nuclei, the following prior knowledge is introduced. First, the nucleus should be surrounding by cytoplasm. Second, if there is only background area around the candidate nuclei, the candidate nuclei is noise. Third, the area of cell (including cytoplasm and nuclei) should be higher than a prespecified value (i.e., 1000). Namely, if the area of a whole cell is lower than the specified value, this region is regarded as noise. The effect of this approach is illustrated in Fig. 3.

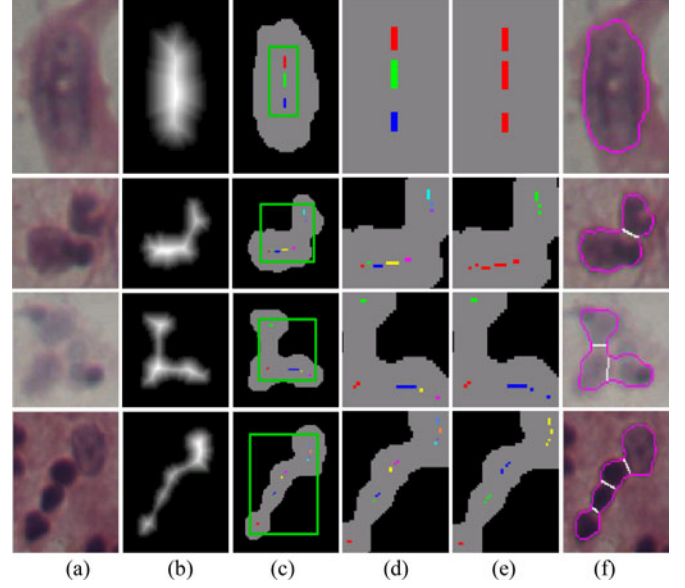


Fig. 4. (a) Original image; (b) inner-distance map; (c) markers obtained from adaptive threshold of inner-distance map; (d) zoomed green box region from (c), noted different markers with different colors; (e) markers after clustering of the (c), same cluster of markers have the same color; (f) results of splitting, nuclei boundaries and splitting lines are marked as pink and white, respectively.

C. Touching Nucleus Splitting by Markers

The MSCN and graph partitioning algorithm given in the previous section can accurately separate cytoplasm, nuclei, and background regions. However, we frequently observe wide ranging degrees of nuclei overlaps in result images. For the quantitative analysis of cervical cell's abnormal degree, a novel robust nuclei clump splitting algorithm is proposed in this section.

Our touching nucleus approach is splitting based on markers, and the number of markers decides if there is any overlapping of nuclei. From Fig. 4, it can be seen that there is no need to determine if there is any overlapping of the nuclei. The nuclei at different stages have different shapes, and hence, avoid the splitting error by the prior judgment error.

1) *Marker Finding*: Since the shape of a cervical nucleus is convex, each center of object's nucleus should have local maximal distances to the boundaries in the overlapping clump. Therefore, the distance transform or inner-distance map is utilized to compute markers corresponding to the center of the nuclei. The inner-distance transform of a nucleus pixel p is defined as

$$D(p) = \min_{q \in E} \|p - q\| \quad (14)$$

where $\|\bullet\|$ is the Euclidean distance and pixel q is an element of the set of nucleus' edge pixels.

To find markers of the image in the inner-distance map, we check the criteria: whether the current pixel value is greater than or equal to any of its neighbors in the 3×3 region. However, the noise point may become a local maximum. To overcome this, a global threshold T is designed to eliminate the impact of

noisy pixels and is given as

$$T = \mu M(p) - (\max_{i \in M} D(i) + \min_{i \in M} D(i) - 2M(p)) \quad (15)$$

$$M(p) = \frac{1}{N} \sum_{i \in M} D(i) \quad (16)$$

where μ is the adjusting parameters, M is the set of markers, and N is the number of pixel i belong to the markers M . As a result, if the marker's distance is smaller than T , it will be removed.

2) *Marker Clustering*: From Fig. 4(c) and (d), we observed that each target can have several markers, and hence, different markers from the same target should be fused into one marker. Differing from the seed filtering, the main difficulty is that the final numbers of the markers are unknown beforehand. In view of this, an unsupervised clustering method is implemented, and the shape and geometrical information are combined together to improve the clustering accuracy on the markers.

In the clustering process, the measure evidence distance between marker m_i and m_j to decide the final clustering effect is defined as

$$g(m_i, m_j) = \min_{p \in m_i, q \in m_j} \|p - q\|. \quad (17)$$

Instead of using hard threshold or grid search, an adaptive threshold is adopted to find conditions in our experiment, which is defined as

$$g(m_i, m_j) \leq \min_{p \in m_i, q \in m_j} (D(p), D(q)). \quad (18)$$

The overlapping nuclei might lose the original distance information with the conventional unsupervised clustering method since the cluster centroids are used as the new clusters. For the proposed method, the original significant marker is kept, and the pixels from the two classes m_i and m_j are clustered as a new cluster, which is shown in Fig. 4(e).

3) *Splitting Based on Shape and Color Information*: After obtaining the correct markers, the simplest way to find the split line between touching objects is to use the nearest-neighbor assignment, which assigns each pixel to its nearest marker. However, this method causes unnatural object boundary and is inaccurate when there are too many variations on the object sizes. Therefore, the gradient-barrier watershed algorithm [40], which incorporates geometric and intensity information to effectively determine the natural boundary is adopted in our method. However, oversegmentation errors occur when the nuclei are poorly stained and internal structure of the nucleus has been modified. To solve this limitation, the effective evidence from pixel to marker association is proposed. The effective evidence $L(p, m_i)$ between pixel p and marker m_i is defined as

$$L(p, m_i) = \eta \|D(p) - \min_{q \in m_i} D(q)\| + v \|I_p - \overline{m_i}\| \quad (19)$$

where I_p is the mean intensity value of the 5×5 patch centered at pixel p , $\overline{m_i}$ is the mean intensity value of marker m_i in the inner-distance map, and η and v are adjusting weight parameters. Finally, the pixel p is assigned by

$$S(p, m_i) = \operatorname{argmin}_{m_i \in \text{markers}} L(p, m_i). \quad (20)$$

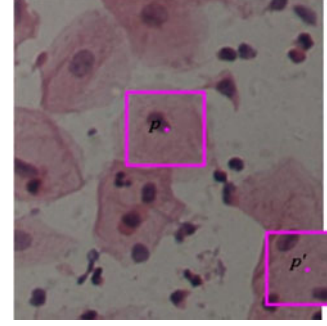


Fig. 5. Illustration of sample train set in image boundaries by mirroring.

IV. EXPERIMENTAL RESULTS

A. Clinical Data Collection

The materials used in our experiments are collected from the Sixth People's Hospital of Shenzhen based on 200 female subjects aged from 22 to 64. All the materials used in this experiment have been approved by the Ethics Committee of the Sixth People's Hospital of Shenzhen, and informed written permission is obtained from each participant. A total of 53 slides are collected using the Olympus BX43 microscope at a magnification rate of 40. 21 images (15 images contain abnormal and 6 images contain normal nuclei only) are chosen for our evaluation. The ground truth of cytoplasm and nucleus segmentation was obtained by manual delineation by a pathologist with more than 15 years of residency. All slides were prepared using a manual liquid-based cytology technique stained with H&E, and confirmed by biopsy.

B. Parameters and Implementation Details

1) *MSCN Feature Extraction*: The MSCN includes three layers. The first two layers are composed of a bank of filter size 11×11 followed by tanh units and 2×2 max-pooling operations, the third layer is the full connection layer. The input image is transformed into the YUV color space, the pyramid includes three different scales: 1024×1360 , 512×680 , and 256×340 . Each pixel is centered in the 32×32 region as the network input. When a pixel is close to the image border, its window will include pixels outside the image boundaries, such pixels are synthesized by mirroring the pixels in the actual image across the boundary (see Fig. 5).

Three different scales, Y, U, V spaces, all nine convolutional network are trained parallel, dimension of the filtering is obtained via grid search. The final Y channel is eight dimensions, U is six dimensions, and V is two dimensions. There are a total of 5 650 background, 8 590 cytoplasm, and 8 560 nucleus pixels as the training sample.

2) *Graph Partitioning*: The SLIC method has two main parameters involved: the area of the superpixels and the balance parameters to control compactness of the superpixel. If the area value is too big, the small nucleus will become invisible. On the other hand, when the value is too small, it will increase the

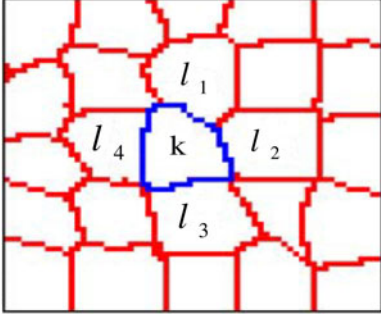


Fig. 6. Illustration of neighboring superpixels.

computation burden and lose the function of voting. Finally, the area value is empirically set as 10.

As for balance parameters, small superpixel regions usually have irregular shapes, whereas big superpixel cannot capture the boundary very well. Thus, this value is set as 0.1 empirically. The neighborhood superpixel is defined as a common edge of these areas (see Fig. 6). Since the superpixel area is set as 10, the perimeter is approximately 12 pixels, the value of common edge is set as 2. To construct the pairwise term, the input image is converted to grayscale image for evaluating the superpixel region's similarity. In our graph, $\lambda = 120$, $\alpha = 0.1$, and $\beta = 20$ obtains the best performance with grid search.

3) *Postprocessing*: For each candidate nucleus clump, the area of each class in the ring region obtained by morphological dilation with the structure element is selected as a disk. A radius of 5 pixels is empirically selected in this paper. If the area ratio of background and cytoplasm is higher than 3, we filter the nucleus clump, and we filter the cell if the whole cell region's area is lower than 1000 pixels.

4) *Touching Nucleus Splitting*: There are three parameters involved to avoid the noise interference. The global threshold T is added if the value is lower than 0, which indicate that most candidate markers have large distance values, and large weight for $M(p)$ should be added for a global threshold T . Based on empirical value and the experiments, μ is set as 0.8.

In the process of splitting, η controls the shape information for the weight in the distance measure $L(p, m_i)$, v is the weight for the color information. The color information is calculated based on the R, G, and B channels and get the sum values. η and v is set as 0.8 and 0.2 by cross validation, respectively.

C. Evaluation of Cytoplasm Segmentation

1) *Evaluation Metric*: Full resolution images consist of multiple cells, hence, a matching step is required to find the correspondences between the resulting segments and the ground truth. However, reliable delineation of the cytoplasm boundary for each cell is unrealistic even for human experts in the presence of heavily overlapping cells. Therefore, the dice similarity coefficient (DSC) [50] is used to evaluate the performance as follows:

$$\text{DSC} = 2 \frac{|A_{\text{GT}} \cap A_{\text{seg}}|}{|A_{\text{GT}}| + |A_{\text{seg}}|} \quad (21)$$

TABLE I
MEAN AND STANDARD DEVIATION OF DSC OF CYTOPLASM SEGMENTATION
PERFORMANCE COMPARISON BETWEEN PROPOSED METHOD AND OTHER
METHODS

	[12]	[8]	Ours
Mean	0.64	0.93	0.95
Std.	0.26	0.3	0.18

TABLE II
COMPARISON OF AVERAGE NUCLEUS BINARIZATION PERFORMANCE USING
PIXEL-BASED CRITERION

Method	All Nuclei				Abnormal Nuclei			
	PPV	NPV	F1	Ovel	PPV	NPV	F1	Ovel
[16]	0.52	0.77	0.598	0.45	0.62	0.86	0.688	0.56
[51]	0.79	0.67	0.710	0.57	0.77	0.61	0.627	0.52
[8]	0.85	0.90	0.873	0.78	0.88	0.91	0.884	0.81
Ours	0.94	0.92	0.912	0.87	0.90	0.91	0.897	0.83

TABLE III
COMPARISON OF AVERAGE NUCLEUS BINARIZATION PERFORMANCE USING
OBJECT-BASED CRITERION

	[16]	[51]	[8]	Ours
Mean	0.80	0.78	0.99	0.99
Std.	0.35	0.14	0.01	0.01

where A_{GT} and A_{seg} denote the manual “ground truth” and the segmented cytoplasm, respectively, $|\bullet|$ is the number of pixels in a certain region $\text{DSC} \in [0, 1]$. A higher DSC value indicates better segmentation performance.

2) *Comparison With Other Methods*: The performance of the proposed method is further compared with methods in [8] and [12]. Since both algorithms segment the cytoplasm first, and then, the nucleus, to objectively evaluate the performance, the cytoplasm performance evaluation is based on the common area between nuclei and cytoplasm.

Table I summarizes the mean and standard deviation of the DSC for the selected three methods. Compared with [12], the DSC mean and standard deviation are improved by 48.44% and reduced by 30.77%, respectively, using the proposed method. The reason of degradation with [12] is that the images used in their experiments did not have the abnormal and normal nuclei, and the difference between nuclei and background is quite obscure. The images in [12] have low contrast, poor illumination, and only the color space transform and morphological operation are utilized. These reasons led to poor segmentation performance. The images used in our method are collected automatically without manual intervention. Both normal and abnormal cells exist in our dataset, which enhances the algorithm's generalizability.

Compared with [8], the DSC mean is improved by 2.15%, but the standard deviation is decreased by 40.00%. Although the mean DSC value is not improved significantly, the low standard deviation means that the segmentation performance is

TABLE IV
COMPARISON OF ABNORMAL NUCLEUS BINARIZATION PERFORMANCE
BY GRADING $F1$ -MEASURE

Method	% Poor	% Acceptable	% Very accurate
[16]	45.3	54.7	17.2
[51]	48.4	51.6	20.3
[8]	6.2	93.8	51.6
Ours	9.6	90.4	60.2

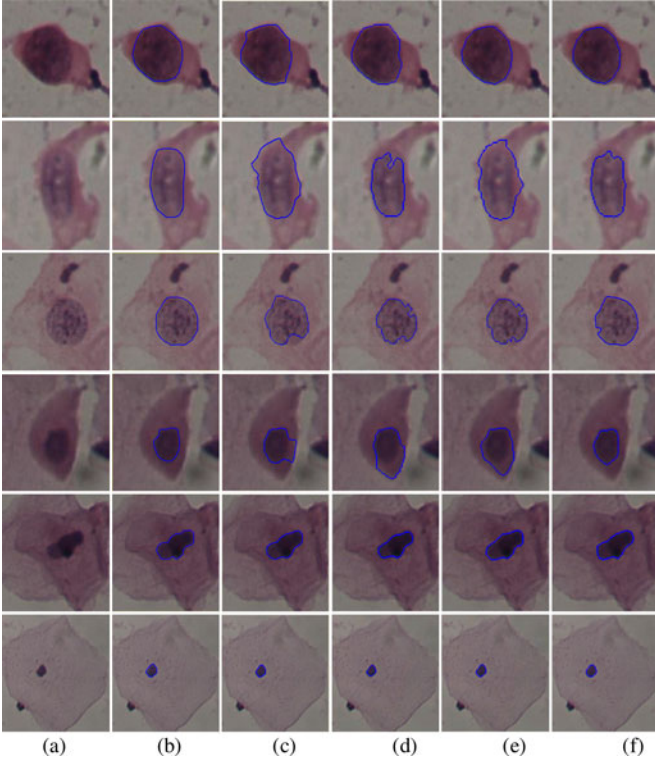


Fig. 7. Comparison of the nuclei segmentation under different algorithms. From left to right: (a) original images, (b) ground truth, (c)–(f) segmentation results by [16], [51], [8], and the proposed method.

relatively stable as compared to the method in [8]. Also, there is no color selection and noise filtering, which is more generalized compared with that with it.

D. Evaluation of Nuclei Segmentation

1) *Evaluation Metric*: To evaluate nucleus segmentation, a pixel-based and object-based criterion is used. In the pixel-based criterion, the positive predictive value (PPV), negative predictive value (NPV), $F1$ measurement ($F1$), and overlapping ratio ($Ovel$) are adopted for the objective evaluation of the segmentation ratio. These metrics can be used to evaluate all the nuclei in the image and each abnormal nucleus individually. Moreover, the pixel-based criterion serves as a basis for designing the object-based criterion. Nucleus detection was considered as a true positive if its NPV was higher than 60%.

To better evaluate the segmentation performance of the abnormal nucleus, we graded the $F1$ values, $F1$ value below 0.75

TABLE V
EVALUATION OF SPLITTING PERFORMANCE

Image ID	No. cells	Correct split	Under Split	Over Split	Error	PPV	NPV
1	104	97	4	0	2	1.000	0.960
2	68	62	2	1	1	0.984	0.969
3	72	67	3	0	1	1.000	0.957
4	107	105	1	0	0	1.000	0.991
5	75	73	1	0	0	1.000	0.986
6	62	50	5	1	3	0.980	0.909
7	198	184	6	1	3	0.995	0.968
8	144	133	5	0	3	1.000	0.964
9	86	81	3	0	1	1.000	0.964
10	61	58	1	0	1	1.000	0.983
11	384	353	20	1	6	0.997	0.946
12	85	81	1	2	0	0.976	0.988
13	296	274	10	2	8	0.993	0.965
14	236	227	7	0	2	1.000	0.970
15	287	265	15	1	6	0.996	0.946
16	261	237	20	2	2	0.992	0.922
17	391	366	21	0	4	1.000	0.946
18	346	307	26	1	8	0.997	0.950
19	171	158	10	0	2	1.000	0.940
20	157	145	8	0	1	1.000	0.948
21	75	65	4	1	1	0.985	0.942
Total	3666	3388	173	13	55	0.996	0.951
Percentage		92.42	4.72	0.36	1.50		

is unacceptable, above 0.75 is acceptable, and between 0.9 and 1 is very accurate, and then, calculated the percentage of the number of abnormal nuclei in each range. The percentage is summarized in Table IV.

2) *Comparison With Other Methods*: The performance is also compared with the related works [8], [16], [51]. Table II shows the average nucleus binarization performance using pixel based criterion. Compared with [16], $F1$ and $Ovel$ exhibit improvement of 52.51% and 93.33%, respectively, which shows the superiority of the proposed method over the existing methods for pathological and normal nucleus segmentation.

Table III compares average nucleus binarization performance using object-based criterion. Compared with [16], it can be observed that the mean value is improved by 23.75% among all the evaluation, and the mean value is improved by 250.00%. The accepted ratio is improved by 65.27%, and the unaccepted ratio is decreased by 78.81% as shown in Table IV.

The improvement of the proposed method is attributed to its high suitability for single nucleus segmentation, and hence, the contrast between cytoplasm and nucleus is very obvious. In the full resolution image, the uneven stain, various life span of the nucleus, the decreasing ratio of different nucleus increases the challenges of segmentation even for an expert based on contextual information of a small region. Meanwhile, the multiscale technique increases the number of large contextual window and segmentation accuracy.

Similar to our method, Zhang *et al.* [8] and Al-Kofahi *et al.* [51] employed the graph partitioning method based on the Poisson distribution assumption. It can be seen that $F1$ and $Ovel$ are improved by 4.47% and 11.54% compared with [8], respectively. Besides, the proposed method is superior over the abnormal nuclei segmentation, and is slightly better than method in

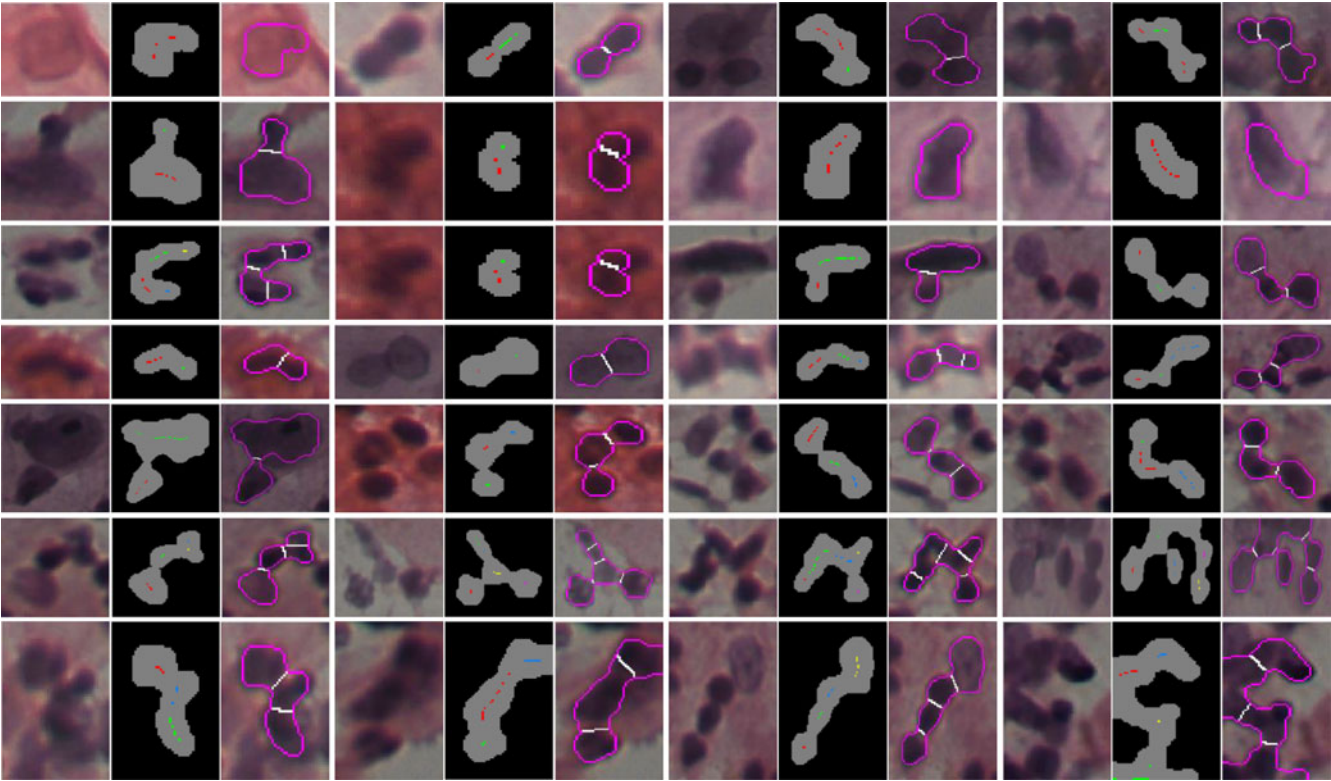


Fig. 8. Examples of splitting touching cell clumps: for each triplet, right image corresponds to the split result for each candidate nuclei, middle image corresponds to the final markers, left image is the original image. Note that some images have been rescaled for better viewing.

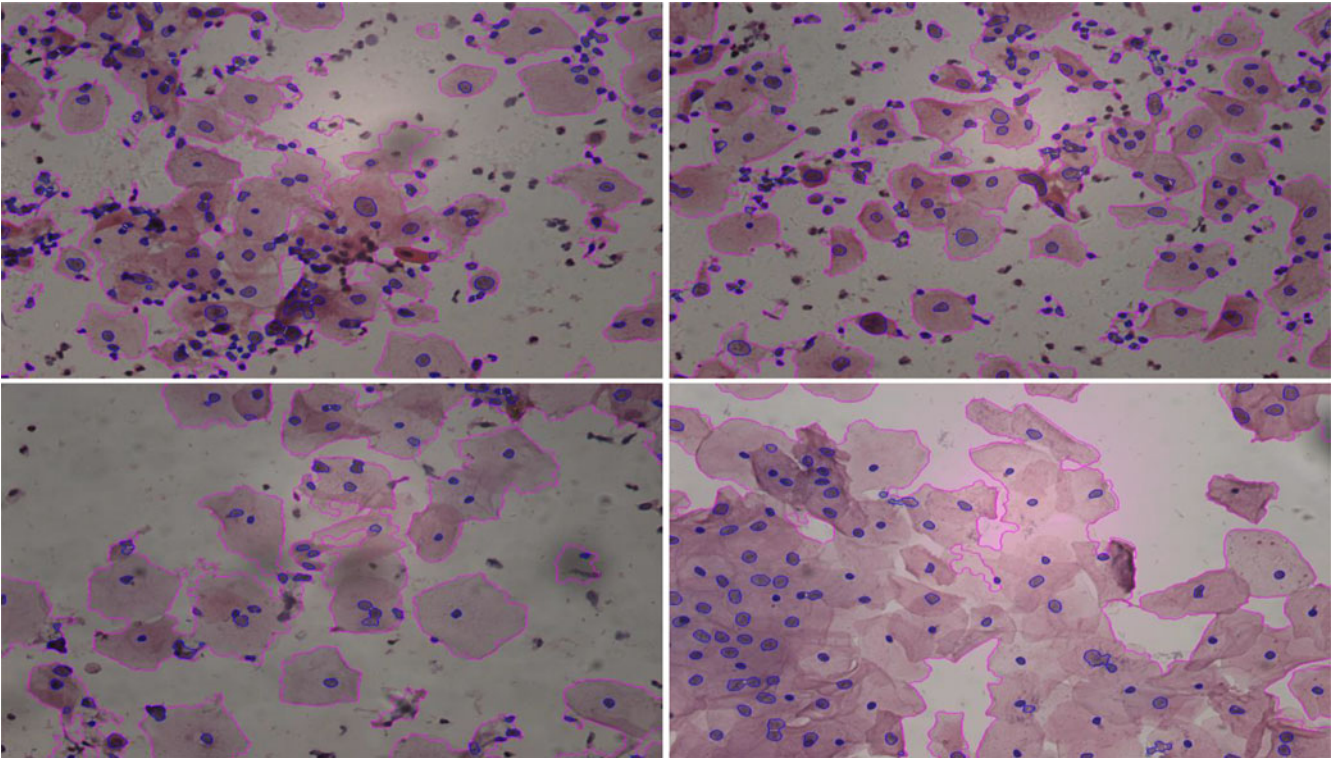


Fig. 9. Automatic segmentation results for full cervical cell images. Upper two images contain abnormal cells, while lower two are normal cases. Boundaries of the cytoplasm and nuclei and the split lines are marked as pink, blue, and white, respectively.

TABLE VI
PERFORMANCE OF OUR SEGMENTATION ALGORITHM USING PIXEL-BASED
CRITERION

Method	Cytoplasm		Nuclei	
	Mean	Std.	Mean	Std.
SSCN	0.62	0.34	0.57	0.32
MSCN	0.79	0.18	0.77	0.22
MSCN + superpixels	0.83	0.17	0.79	0.24
MSCN + graph partitioning	0.90	0.21	0.85	0.18

TABLE VII
RESULT OF SPLITTING ALGORITHM

Algorithm	Correct split	Under Split	Over Split	Error
Classical clustering + effective distance	61.6%	8.1%	3.2%	27.1%
Our clustering + shape information	79.4%	4.4%	1.2%	15.0%
Our clustering + effective distance	90.2%	4.4%	1.2%	4.2%

[16]. The accurate ratio is improved by 16.67%, the acceptable ratio is improved by 3.62%, and the unacceptable ratio is improved by 54.84%. The main reason for the good performance in [8] confirms the effectiveness of the coarse to fine segmentation algorithm. The performance improvement in [8] is due to the introduction of the graph partitioning, which improves both the local and global learning ability.

Compared to [51], *F1* and *Ovel* are improved by 28.45% and 52.63%, respectively. This method is also superior over the abnormal nuclei segmentation, and slightly better than method in [16]. The high accurate ratio is improved by 196.55%, the acceptable ratio is improved by 75.19%, and the unacceptable ratio is improved by 80.17%.

Fig. 7 shows six sample results by [8], [16], and [51] and the proposed method. The proposed method achieves good segmentation performance even under low contrast, highly overlapping, and poor stained cases. The comparisons under different cases demonstrate the superiority of our proposed method over existing methods. The preliminary explanation is that the hierarchical architectures enhance internal representation with the learned robust feature. The MSCN not only increases large contextual window, but also integrates numerous contextual information to globalize the graph partitioning. These techniques increase consistency of superpixel regions for segmentation, and hence, the proposed algorithm obtains better performance.

E. Evaluation of Splitting

Under-splitting, over-splitting, and encroachment errors are selected to evaluate the performance of the splitting of touching nucleus. Under splitting refers to no splitting for the overlapping nucleus, over splitting refers to placement of a boundary within a single nontouching cell, and the encroachment error refers to incorrect nucleus splitting. Table V illustrates the segmentation results based on a total of 21 images. The experimental results based on the average results of three pathological doctors are also presented here.

In a total of 21 images, the image IDs: 1, 2, 3, 4, 5, 6, 9, 10, 12, and 21 are slightly overlapped images with a few nuclei. The total nucleus numbers are less than 107, and the touching nuclei is less than 20. In the touching nuclei, most of them have less than five nuclei, and only a few of them have 7–10 nuclei. The worst segmentation result is image ID 6, 52 out of 62 nuclei are split correctly, whereas others achieved more than 91.18% splitting rate.

Image IDs: 7, 8, 14, 16, 19, and 20 have slightly overlapping nuclei, and the true nuclei is within 144 ~ 261. With the increase of the touching nuclei, the overlapping becomes more complicated. Image ID 14 produces the best results, and the true nuclei is within 144 ~ 261. The correct splitting ratio is 96.19%, the worst ratio of 90.80% is obtained with image ID 16, and the average splitting ratio is 92.84%.

The rest of the images (IDs: 11, 13, 15, 17, and 18) have heavily overlapped nuclei, the true numbers of nuclei is between 287 and 391, the overlapping nuclei is more than 35, and the overlapping cases are quite complicated. For this image, the best performance is 93.61%, the worst is 88.73%, and the average is 91.83%. Fig. 8 shows numerous examples of split touching clumps, and it is clear that the proposed method satisfies the cervical overlapping nuclei's splitting requirement for quantitative analysis of cervical cell's abnormal degree.

Fig. 9 shows four full-segmented images where the upper two images are abnormal images and the bottom images are normal images. Regarding the overlapping of nuclei, the upper two images contain intermediate touching, whereas the bottom two images contain just slightly overlapping. It can be seen that the proposed method addresses the segmentation problem even in the poor-illuminated case. For the low contrast, the proposed method achieves great segmentation performance under inappropriate staining. In the nuclei detection, most of the nuclei are detected correctly. For the touching nuclei splitting, less than four nuclei touching cases can be split effectively. From the aforementioned statistics, the proposed method not only accurately segments the cytoplasm and nucleus, but also accurately separates the touching nuclei, which will be quite beneficial for the cervical cancer screening.

V. DISCUSSIONS

A. Effect of MSCN

Although the CNN can complete the image segmentation task, the traditional CNN has large window size, which leads to high computational cost. A small window can only provide poor observation basis and lead to low classification accuracy. In view of these observations, the spatial pyramid is adopted in our method to preserve more textual, shape, and contextual information without changing window size parameter than a single window. Table VI shows the segmentation accuracy of SSCN alone, MSCN, and MSCN with superpixels and graph-partitioning method. In terms of DSC, the MSCN statistical results shows segmentation performance is improved by 27.42%, and the nucleus segmentation accuracy is improved by 35.09% compared with SSCN, and hence, the MSCN is able to improve the segmentation performance.

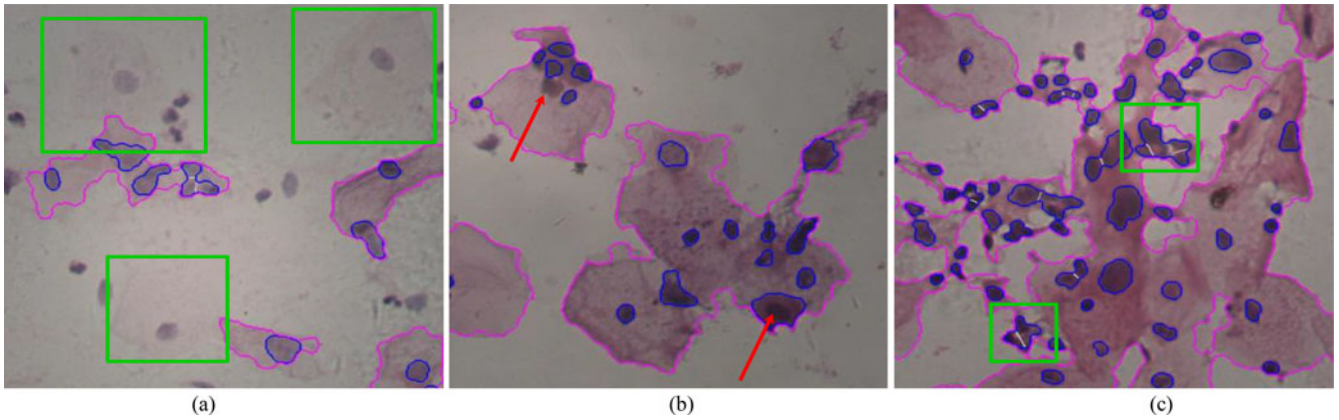


Fig. 10. Examples of failure by our method: (a) erroneous segmentation of some cytoplasm due to poor staining and contrast (green box), (b) erroneous segmentation of some nuclei (red arrow), (c) erroneous split line (green box).

B. Effect of Superpixel

The MSCN is capable of increasing the field-of-view to obtain texture, shape, and context information. The superpixel method is an effective way and standard approach. By using the superpixel, the cytoplasm segmentation accuracy is improved by 5.06%, the nucleus segmentation accuracy is improved by 2.60%. Therefore, the superpixel has a positive effect on the segmentation performance.

C. Effect of Graph Partitioning

To further improve the segmentation performance, the graph-partitioning method is integrated. Superpixel replaces the pixel to reduce the computation time, and the limited local learning ability is improved by integrating global learning ability. After graph partitioning, the performance is further improved, the consistency of the neighboring superpixel is further improved as well.

As shown in Table VI, the cytoplasm performance is improved by 13.92%, and the nucleus segmentation accuracy is enhanced by 10.39%, respectively, using graph partitioning.

D. Effect of Marker and Clustering

A new marker usually poses a representation problem in unsupervised clustering, and the fused clustering distance is used as the new clustering center. But this method ignores the original distance information, which leads to the new clustering center unable to satisfy the marker generation since the location of the new distance is not the local maximum. Consequently, the new generated maker cannot effectively reflect the single target object information, and hence, the spitting error occurs and the object boundary becomes unnatural.

This problem is improved by keeping the distance information of the original maker. Because there is no hard threshold for the fusion condition between different markers, this enhanced clustering algorithm is generalized. To validate the effectiveness of the splitting algorithm, 2000 nucleus clumps are selected to compare the splitting performance, and the results are summarized in Table VII. Table VII confirms that splitting performance

is improved by 46.43% and the splitting line error is decrease by 84.50%.

E. Effect of Effective Distance by Color Information

After obtaining the correct markers, the direct way is to use the nearest-neighbor assignment, but the detected nucleus boundary is unnatural and the splitting performance is very bad. To address this, both shape and color information is included, and weights for shape and color are cross validated.

Table VII gives the results of the effective distance and the traditional geometrical distance result. By using the measure distance, the performance is boosted by 13.60%, and the splitting error is reduced by 72.0%.

F. Failure Cases

One of the limitations of our method is the ignorance of the overlapping cytoplasm splitting. As shown in Fig. 10, the cytoplasm overlapping is highly complicated, and even the clinicians have difficulty to split them correctly. The cytoplasm is beneficial for the cervical diagnosis, but the nucleus information is even more important. For the cytoplasm segmentation, the first limitation is that it is ineffective for the poorly stained cytoplasm. Due to the relatively low ratio of the cytoplasm around the nucleus, the nucleus will be regarded as the impurities, and hence, the nucleus in the green box in Fig. 10 is regarded as background.

The second limitation is the inaccurate segmentation of the atrophic cell since this cell has large overlapping area with other cells, which can be seen in Fig. 10(b). This error is mainly caused by insufficient training samples, and the selected nucleus will be overlapped with other nucleus, as illustrated in Fig. 10(b). The cytoplasm and nucleus are very near; hence the local boundary of the nucleus may be unclear, which leads to the incorrect nucleus segmentation. To resolve this issue, more training samples can be used to further enhance the nucleus segmentation performance.

The third limitation is the overlapping nucleus with complicated shapes, which degrades the splitting performance. As

shown in Fig. 10(c), the left bottom box represents the inaccurate segmentation of nucleus causes incorrect splitting error. The right upper box denotes the inaccurate marker leads to inaccurate segmentation.

VI. CONCLUSION

In this paper, graph partitioning via superpixel and MSCN techniques was investigated for accurate cytoplasm and nucleus segmentation in the cervical image. Our experimental results indicated that superpixel, graph partitioning, and MSCN are highly effective for cervical cell segmentation. The achieved remarkable segmentation results demonstrate that the proposed method can be used for automatic cervical cancer detection and diagnosis. Compared with previous algorithms, state-of-the-art performance is achieved. Moreover, the proposed method is a promising way for cervical cancer screening and provides powerful support for automatic assisting.

REFERENCES

- [1] A. Jemal *et al.*, "Global cancer statistics," *CA-Cancer J. Clin.*, vol. 61, pp. 69–90, 2011.
- [2] W. H. O. R. Health, W. H. O. C. Diseases, and H. Promotion, *Comprehensive Cervical Cancer Control: A Guide to Essential Practice*, World Health Organization, Geneva, Switzerland, 2006.
- [3] J. Ferlay *et al.*, "Estimates of worldwide burden of cancer in 2008: GLOBOCAN 2008," *Int. J. Cancer*, vol. 127, pp. 2893–2917, 2010.
- [4] D. Saslow *et al.*, "American cancer society, American society for colposcopy and cervical pathology, and American society for clinical pathology screening guidelines for the prevention and early detection of cervical cancer," *CA-Cancer J. Clin.*, vol. 62, pp. 147–172, 2012.
- [5] G. G. Birdsong, "Automated screening of cervical cytology specimens," *Hum. Pathol.*, vol. 27, pp. 468–481, 1996.
- [6] E. Bengtsson, "Computerized cell image analysis: Past, present, and future," in *Image Analysis*. New York, NY, USA: Springer, 2003, pp. 395–407.
- [7] E. Bengtsson, "Recognizing signs of malignancy—The quest for computer assisted cancer screening and diagnosis systems," in *Proc. Int. Conf. Comput. Intell.*, 2010, pp. 1–6.
- [8] L. Zhang *et al.*, "Segmentation of cytoplasm and nuclei of abnormal cells in cervical cytology using global and local graph cuts," *Comput. Med. Imag. Graph.*, vol. 38, pp. 369–380, 2014.
- [9] Y. Marinakis *et al.*, "Pap smear diagnosis using a hybrid intelligent scheme focusing on genetic algorithm based feature selection and nearest neighbor classification," *Comput. Biol. Med.*, vol. 39, pp. 69–78, 2009.
- [10] O. Lezoray and H. Cardot, "Cooperation of color pixel classification schemes and color watershed: A study for microscopic images," *IEEE Trans. Image Process.*, vol. 11, no. 7, pp. 783–789, Jul. 2002.
- [11] M.-H. Tsai *et al.*, "Nucleus and cytoplasm contour detector of cervical smear image," *Pattern Recogn. Lett.*, vol. 29, pp. 1441–1453, 2008.
- [12] A. Gençtav, S. Aksoy, and S. Önder, "Unsupervised segmentation and classification of cervical cell images," *Pattern Recogn.*, vol. 45, pp. 4151–4168, 2012.
- [13] L. Zhang *et al.*, "Automation-assisted cervical cancer screening in manual liquid-based cytology with hematoxylin and eosin staining," *Cytometry A*, vol. 85, no. 3, pp. 214–230, 2014.
- [14] S.-F. Yang-Mao *et al.*, "Edge enhancement nucleus and cytoplasm contour detector of cervical smear images," *IEEE Trans. Syst., Man, Cybern. B, Cybern.*, vol. 38, no. 2, pp. 353–366, Apr. 2008.
- [15] P. Bamford and B. C. Lovell, "A water immersion algorithm for cytological image segmentation," in *Proc. APRS Image Segmentation Workshop*, 1996, pp. 75–79.
- [16] K. Li *et al.*, "Cytoplasm and nucleus segmentation in cervical smear images using radiating GVF snake," *Pattern Recogn.*, vol. 45, pp. 1255–1264, 2012.
- [17] C. Bergmeir *et al.*, "Segmentation of cervical cell nuclei in high-resolution microscopic images: A new algorithm and a web-based software framework," *Comput. Method. Program. Biomed.*, vol. 107, pp. 497–512, 2012.
- [18] M. E. Plissiti *et al.*, "Automated detection of cell nuclei in pap smear images using morphological reconstruction and clustering," *IEEE Trans. Inf. Technol. Biomed.*, vol. 15, no. 2, pp. 233–241, Mar. 2011.
- [19] M. E. Plissiti *et al.*, "Combining shape, texture and intensity features for cell nuclei extraction in Pap smear images," *Pattern Recogn. Lett.*, vol. 32, pp. 838–853, 2011.
- [20] H.-S. Wu *et al.*, "A parametric fitting algorithm for segmentation of cell images," *IEEE Trans. Biomed. Eng.*, vol. 45, no. 3, pp. 400–407, Mar. 1998.
- [21] P. Bamford and B. Lovell, "Unsupervised cell nucleus segmentation with active contours," *Signal Process.*, vol. 71, pp. 203–213, 1998.
- [22] C. Farabet *et al.*, "Learning hierarchical features for scene labeling," *IEEE Trans. Pattern Anal. Mach. Intell.*, vol. 35, no. 8, pp. 1915–1929, Aug. 2013.
- [23] B. B. Le Cun *et al.*, "Handwritten digit recognition with a back-propagation network," in *Proc. Neural Inf. Process. Syst.*, 1990, pp. 396–404.
- [24] Y. LeCun *et al.*, "Gradient-based learning applied to document recognition," *Proc. IEEE*, vol. 86, no. 11, pp. 2278–2324, Nov. 1998.
- [25] V. Jain *et al.*, "Supervised learning of image restoration with convolutional networks," in *Proc. Conf. Comput. Vis.*, 2007, pp. 1–8.
- [26] B. Pang *et al.*, "Cell nucleus segmentation in color histopathological imagery using convolutional networks," in *Proc. Chin. Conf. Pattern Recogn.*, 2010, pp. 1–5.
- [27] D. Ciresan *et al.*, "Deep neural networks segment neuronal membranes in electron microscopy images," in *Proc. Neural Inf. Process. Syst.*, 2012, pp. 2843–2851.
- [28] S. C. Turaga *et al.*, "Convolutional networks can learn to generate affinity graphs for image segmentation," *Neural Comput.*, vol. 22, pp. 511–538, 2010.
- [29] D. Padfield *et al.*, "Spatio-temporal cell cycle phase analysis using level sets and fast marching methods," *Med. Imag. Anal.*, vol. 13, pp. 143–155, 2009.
- [30] S. Ali and A. Madabhushi, "An integrated region-, boundary-, shape-based active contour for multiple object overlap resolution in histological imagery," *IEEE Trans. Med. Imag.*, vol. 31, no. 7, pp. 1448–1460, Jul. 2012.
- [31] P. F. Felzenszwalb and D. P. Huttenlocher, "Efficient graph-based image segmentation," *Int. J. Comput. Vis.*, vol. 59, pp. 167–181, 2004.
- [32] J. Shi and J. Malik, "Normalized cuts and image segmentation," *IEEE Trans. Pattern Anal. Mach. Intell.*, vol. 22, no. 8, pp. 888–905, Aug. 2000.
- [33] A. Lucchi *et al.*, "Supervoxel-based segmentation of mitochondria in em image stacks with learned shape features," *IEEE Trans. Med. Imag.*, vol. 31, no. 2, pp. 474–486, Feb. 2012.
- [34] A. Delong and Y. Boykov, "Globally optimal segmentation of multi-region objects," in *Proc. Int. Conf. Comput. Vis.*, 2009, pp. 285–292.
- [35] Y. Y. Boykov and M.-P. Jolly, "Interactive graph cuts for optimal boundary & region segmentation of objects in ND images," in *Proc. Int. Conf. Comput. Vis.*, 2001, pp. 105–112.
- [36] Y. Boykov and V. Kolmogorov, "An experimental comparison of min-cut/max-flow algorithms for energy minimization in vision," *IEEE Trans. Pattern Anal. Mach. Intell.*, vol. 26, no. 9, pp. 1124–1137, Sep. 2004.
- [37] X. Lou *et al.*, "Learning to segment dense cell nuclei with shape prior," in *Proc. Int. Conf. Comput. Vis. Pattern Recogn.*, 2012, pp. 1012–1018.
- [38] H. Chang *et al.*, "Invariant delineation of nuclear architecture in Glioblastoma multiforme for clinical and molecular association," *IEEE Trans. Med. Imag.*, vol. 32, no. 4, pp. 670–682, Apr. 2013.
- [39] J. Cheng and J. C. Rajapakse, "Segmentation of clustered nuclei with shape markers and marking function," *IEEE Trans. Biomed. Eng.*, vol. 56, no. 3, pp. 741–748, Mar. 2009.
- [40] H. Yang and N. Ahuja, "Automatic segmentation of granular objects in images: Combining local density clustering and gradient-barrier watershed," *Pattern Recogn.*, vol. 47, pp. 2266–2279, 2014.
- [41] N. Jamil *et al.*, "A modified edge-based region growing segmentation of geometric objects," in *Visual Informatics: Sustaining Research and Innovations*. New York, NY, USA: Springer, 2011, pp. 99–112.
- [42] M. E. Plissiti and C. Nikou, "Overlapping cell nuclei segmentation using a spatially adaptive active physical model," *IEEE Trans. Image Process.*, vol. 21, no. 11, pp. 4568–4580, Nov. 2012.
- [43] C. Park *et al.*, "Segmentation, inference and classification of partially overlapping nanoparticles," *IEEE Trans. Pattern Anal. Mach. Intell.*, vol. 35, no. 3, pp. 669–681, Mar. 2013.

- [44] P. Quelhas *et al.*, "Cell nuclei and cytoplasm joint segmentation using the sliding band filter," *IEEE Trans. Med. Imag.*, vol. 29, no. 8, pp. 1463–1473, Aug. 2010.
- [45] H. Kong *et al.*, "Partitioning histopathological images: An integrated framework for supervised color-texture segmentation and cell splitting," *IEEE Trans. Med. Imag.*, vol. 30, no. 9, pp. 1661–1677, Sep. 2011.
- [46] H. Fatakdwala *et al.*, "Expectation maximization driven geodesic active contour with overlap resolution (emagacor): Application to lymphocyte segmentation on breast cancer histopathology," *IEEE Trans. Biomed. Eng.*, vol. 57, no. 7, pp. 1676–1689, Jul. 2010.
- [47] L. Zhang *et al.*, "Automation-assisted cervical cancer screening in manual liquid-based cytology with hematoxylin and eosin staining," *Cytometry A*, vol. 85, pp. 214–230, 2014.
- [48] R. Achanta *et al.*, "SLIC superpixels compared to state-of-the-art superpixel methods," *IEEE Trans. Pattern Anal. Mach. Intell.*, vol. 34, no. 11, pp. 2274–2282, Nov. 2012.
- [49] Y. Boykov *et al.*, "Fast approximate energy minimization via graph cuts," *IEEE Trans. Pattern Anal. Mach. Intell.*, vol. 23, no. 11, pp. 1222–1239, Nov. 2001.
- [50] L. R. Dice, "Measures of the amount of ecologic association between species," *Ecology*, vol. 26, pp. 297–302, 1945.
- [51] Y. Al-Kofahi *et al.*, "Improved automatic detection and segmentation of cell nuclei in histopathology images," *IEEE Trans. Biomed. Eng.*, vol. 57, no. 4, pp. 841–852, Apr. 2010.

Authors' Photographs and biographies not available at the time of publication.